

Synthesis of Paracrystalline Diamond

Howard Sheng (✉ hsheng@gmu.edu)

George Mason University

Hu Tang

Center for High Pressure Science and Technology Advanced Research <https://orcid.org/0000-0003-1571-8843>

Xiaohong Yuan

Center for High Pressure Science and Technology Advanced Research

Yong Cheng

Department of Materials Science and Engineering, College of Materials, Xiamen University

Hongzhan Fei

Universität Bayreuth <https://orcid.org/0000-0003-3143-7363>

Fuyang Liu

Center for High Pressure Science and Technology Advanced Research

Tao Liang

Center for High Pressure Science and Technology Advanced Research

Zhidan Zeng

Center for High Pressure Science and Technology Advanced Research <https://orcid.org/0000-0003-4283-2393>

Takayuki Ishii

Center for High Pressure Science and Technology Advanced Research <https://orcid.org/0000-0002-1494-2141>

Mingsheng Wang

Xiamen University <https://orcid.org/0000-0003-3754-2850>

Tomoo Katsura

University of Bayreuth

Huiyang Gou

Center for High Pressure Science and Technology Advanced Research

Physical Sciences - Article

Keywords: paracrystalline diamond, amorphous materials, solids

Posted Date: May 7th, 2021

DOI: <https://doi.org/10.21203/rs.3.rs-438542/v1>

License:  This work is licensed under a Creative Commons Attribution 4.0 International License.

[Read Full License](#)

Version of Record: A version of this preprint was published at Nature on November 24th, 2021. See the published version at <https://doi.org/10.1038/s41586-021-04122-w>.

Synthesis of Paracrystalline Diamond

Hu Tang¹, Xiaohong Yuan¹, Yong Cheng², Hongzhan Fei³, Fuyang Liu¹, Tao Liang¹, Zhidan Zeng¹, Takayuki Ishii³, Ming-Sheng Wang², Tomoo Katsura³, Howard Sheng^{4,*}, Huiyang Gou^{1,5,*}

¹Center for High Pressure Science and Technology Advanced Research, Beijing 100094, China

²Department of Materials Science and Engineering, College of Materials, Xiamen University, Xiamen, Fujian 361005, China

³Bayerisches Geoinstitut, Universität Bayreuth, Bayreuth D95440, Germany

⁴Department of Physics and Astronomy, George Mason University, Fairfax 22030, USA

⁵College of Environmental and Chemical Engineering, Yanshan University, Qinhuangdao 066004, Hebei, China

*Corresponding authors: Howard Sheng (hsheng@gmu.edu), Huiyang Gou (huiyang.gou@hpstar.ac.cn)

Solids in nature can be generally classified into crystalline and non-crystalline states¹⁻⁷, depending on whether long-range lattice periodicity is present in the material. The differentiation of the two states, however, could face fundamental challenges if the degree of long-range order in crystals is significantly reduced. Here we report a unique paracrystalline state of diamond that is distinct from either crystalline or amorphous diamond⁸⁻¹⁰. The paracrystalline diamond reported in this work, consisting of sub-nanometer-sized paracrystals that possess a well-defined crystalline medium-range order up to a few atomic shells^{4,5,11-14}, was synthesized in high-pressure high-temperature conditions (e.g., 30 GPa, 1600 K) employing fcc-C₆₀ as a precursor. The structural characteristics of paracrystalline diamond was identified through a combination of X-ray diffraction, high-resolution transmission microscopy, and advanced molecular dynamics simulation. The formation of paracrystalline diamond is a result of densely distributed nucleation sites developed in compressed C₆₀ as well as pronounced second-nearest-neighbor short-range order in amorphous diamond due to strong *sp*³ bonding. The discovery of paracrystalline diamond adds a new diamond form to the enriched carbon family¹⁵⁻¹⁷, which exhibits distinguishing physical properties and can be furthered exploited to develop new materials. Furthermore, this work reveals the missing link in the length-scale between amorphous and crystalline states across the structural landscape, which has profound implications for recognizing complex structures arising from amorphous materials.

Amorphous solids refer to materials that do not possess long-range periodicity as exhibited in crystals¹⁻¹¹. Consequently, Bragg peaks associated with crystalline arrangements of atoms are absent or obscured in the diffraction signals of amorphous materials, which renders the recognition of their structural organizations notoriously difficult. Due to decades of research effort, it is now understood that structural ordering on the atomic level of amorphous solids is ubiquitous, as manifested by the short-to-medium-range ordering in metallic glasses⁵⁻⁷ and the continuous-random networks (CRN) of amorphous semiconductors¹⁻³. Moving from the short range into the extended length-scale abutting the long-range scale, however, our understanding of the structural arrangements remains much more limited, and it is often complicated by capricious crystalline structural ordering encountered in amorphous materials^{14,18-20}. In an attempt to resolve this structural enigma, a paracrystalline structure model was proposed^{11,20}, in which nanosized paracrystals, defined as severely distorted crystals, were introduced to the amorphous matrix to account for the crystalline medium range order (MRO). A crucial question to answer is, in the configurational space, are we able to identify a state of matter that is fully packed with tiny paracrystals possessing only MRO but devoid of long-range order (LRO)? The identification of such a material state is essential to obtaining much-needed structural information differentiating amorphous solids with and without crystalline MRO. This material state with dominating crystalline MRO, in connection with truly amorphous solids and crystalline solids with LRO, would serve as the Rosetta stone to uncover the nature of a large set of non-crystalline materials. In this work, we report the discovery of such a substance in diamond, termed paracrystalline diamond (p-D).

Among myriads of carbon allotropes, diamond stands out as an important industrial material, featuring complete sp^3 bonding. Diamond exists in many crystal forms, among which the most familiar are cubic diamond (CD) and hexagonal diamond (HD). Synthesizing diamonds with novel structures¹⁷ and functionalities from sp^2 -bonded carbon has been an actively pursued research theme. However, unlike other fourfold-coordinated systems such as Si and Ge, synthesis of fully sp^3 -bonded amorphous carbon, or amorphous diamond (a-D), has proven difficult. Chemical vapor deposition (CVD) and physical sputtering methods, approaches for forming amorphous Si (a-Si) or Ge (a-Ge), only result in diamond-like carbon (DLC) with variable sp^3 fractions, which is interesting in its own right because of its useful combinations of mechanical, optical, electrical, and chemical properties²¹. Not until recently was Zeng *et al.* able to synthesize recoverable a-D by means of laser heating in a diamond-anvil cell (DAC)⁹. Structure-wise, the as-obtained a-D can be described by the CRN model, in line with other tetrahedral amorphous systems. It was also reported that a-D can be produced by shock compression involving highly nonequilibrium high-pressure and high-temperature (HP-HT) conditions⁸.

The current realization of a-D requires relatively high pressure (40-55 GPa) and a rapid cooling rate (10^6 - 10^{10} K/s)^{8,9}, and the finite sample size (several tens of μm) inevitably hampers our understanding of the structure, properties, and synthesis mechanism. As such, synthesizing large and high-quality a-D remains both highly demanding and technically challenging. In this study, we attempted to synthesize mm-sized non-crystalline diamond using a large-volume multi-anvil press (MAP). Conventional MAP technology could not generate such ultrahigh pressures in a mm-sized sample. However, our recently developed ultrahigh-pressure technique using MAP is capable of generating pressures to 50 GPa in mm-sized samples²². Using this technique, we succeeded in synthesizing p-D with a 1.0 mm diameter at a pressure of 30 GPa. We present details regarding the synthesis and structural analyses of this sample and articulate the synthesis mechanism below.

We selected zero-dimensional fullerene (C_{60}) in an fcc crystal to monitor its phase evolution at 30 GPa and a temperature range of 1200-1800 K. The relevance of using C_{60} as the starting material will be addressed in a later section. Previous investigations have demonstrated that C_{60} can only transform into disordered sp^2 - sp^3 carbon under hydrostatic pressures (13-25 GPa) and high temperatures²³⁻²⁶. Here, at an elevated pressure condition of 30 GPa, the X-ray diffraction patterns (XRD) of the recovered samples synthesized at various temperatures are shown in Fig. 1a and Extended Data Fig. 1. The diffraction signals are distinctly different from the initial fcc- C_{60} (Fig. 1b), signaling the formation of new phases. Broadened diffraction peaks around ~ 2.9 , ~ 5.4 , and $\sim 8.4 \text{ \AA}^{-1}$ are reminiscent of amorphous materials, bearing considerable resemblance to those of a-D⁹ and DLC carbon with high-fraction sp^3 bonding²⁵. Moreover, the recovered samples heated above 1400 K are highly transparent (e.g., Fig. 1a inset), suggesting a dense diamond-like (sp^3 -dominated) structure. In order to examine the composition of sp^2 vs. sp^3 in the samples, we utilized Raman and electron energy loss spectroscopy (EELS), both of which are capable of quantitative analysis^{27,28}. Raman and EELS characterizations (Figs. 1c-d and Extended Data Fig. 2) indicate that the sample recovered from 1400 K contains a residual amount ($\sim 5.2\%$) of sp^2 bonding, whereas samples above 1400 K are completely sp^3 -bonded, demonstrating successful synthesis of non-crystalline diamond at a pressure much lower than previously reported^{8,9}. The densities of the samples at 1500 and 1600 K are estimated to be 3.20 and 3.25 g/cm^3 , respectively, based on the plasmon peak energy derived from low-loss EELS (Extended Data Fig. 2), which are close to that of amorphous diamond (3.30 g/cm^3)^{8,9}. Further increasing the synthesis temperature to 1800 K leads to temperature-induced crystallization and nanosized diamond (Extended Data Fig. 1).

The microscopic features of the as-synthesized samples were scrutinized with high-resolution transmission microscopy (HRTEM). The HRTEM images of the recovered samples are shown in Fig. 2a, c, e, and Extended Data Fig. 3 respectively. Lattice fringes associated with LRO are not

found in the HRTEM images, indicating the disordered nature of the samples beyond a certain length (~ 1 nm). We randomly selected small regions (7.0×7.0 nm²) and conducted fast Fourier transformation (FFT) to obtain the scattering signals in the momentum space. The diffuse halos of the FFT patterns corresponding to the selected areas confirm the overall amorphous feature, consistent with the XRD results. On a finer scale, however, visual inspections indicate that the images become more ordered for samples synthesized at elevated temperatures, which is also evidenced by the narrowing FFT rings with increasing temperature. The ordered HRTEM images resemble those of a-Si films and bulk metallic glasses (BMGs) with MRO structures^{18,29,30}, but they differ from the previously reported a-D described with the CRN model⁹. For the samples annealed at 1400-1600 K, a considerable amount of ordered clusters within 0.5-1.0 nm are visible in the HRTEM images. Within the spatial distance of ~ 1.0 nm, two types of lattice fringes are identifiable, which are found to be close to the atomic arrangements along the $[1\bar{1}0]$ and $[010]$ zone-axes of cubic and hexagonal diamonds (CD and HD), respectively, as shown in Fig. 2f. This finding is further validated by the FFT patterns of the selection areas (2.0×2.0 nm²), where the intensified “diffraction” spots matching CD or HD crystalline order are recognizable. Note that both cubic and hexagonal MRO clusters are highly distorted because the inclusive angles (72.1° for cubic and 89.5° for hexagonal) of the lattice fringes deviate from those of pristine CD (70.3°) and HD (90°) crystals³¹. The observed morphology of the as-synthesized non-crystalline diamond is clearly distinguished from a-D, hinting at the formation of crystalline MRO structures dominating the samples.

To uncover the hidden structural ordering in the obtained non-crystalline diamond, we relied on large-scale classical molecular dynamics (MD) simulation³² employing a recently developed realistic angular-dependent potential for carbon³³. To bridge the temporal gap between experiment and simulation, we enabled an adiabatic-bias molecular dynamics (ABMD) technique³⁴ to accelerate the dynamics. Starting from fcc-C₆₀ and mimicking the experimental HP-HT conditions (e.g., 1600 K and 30 GPa), we revealed how the fullerene evolves into the non-crystalline diamond deterministically. Upon the formation of nearly complete sp^3 bonding at 1600 K, small but prolific clusters with CD- and HD-like atomic packing gradually take form. These MRO clusters typically encompass 4-5 atomic shells, henceforth referred to as paracrystals. With prolonged simulation time, the amount of paracrystals increases and eventually saturates at a volume fraction of $\phi = 0.7$, which is rationalized to be the maximum paracrystal content attainable in the given simulation condition. Above a certain threshold (e.g., $\phi = 0.3$), the paracrystals start to interconnect and percolate, which is a distinguishing feature of the material.

The structure factor $S(Q)$ serves as a probe for identifying structural differences of non-crystalline

materials. Subtle but definite differences in the structure factors (e.g., a-D vs. p-D) can be experimentally discriminated for closely related structures. In our computational simulation, we accurately determined $S(Q)$ from the atomistic models based on the Ornstein-Zernike equation³⁵. The comparison of the simulated $S(Q)$ of a-D and p-D ($\phi = 0.7$) is provided in Fig. 3a. While both $S(Q)$ profiles are characteristic of non-crystalline materials, the differences between the two are conspicuous. The main difference is shown in peak intensity variations. For a-D, the intensity of the first main diffraction peak at ($\sim 2.9 \text{ \AA}^{-1}$) is lower than that of the second peak at ($\sim 5.4 \text{ \AA}^{-1}$). In comparison to a-D, as the volume fraction of paracrystals increases, the intensity of the first peak monotonically rises, accompanied by a decrease in the intensity of the second peak (Extended Data Fig. 4a). The intensity ratio of the first peak to the second peak I_1/I_2 is positively correlated to the degree of MRO arrested in the sample. This relationship is thus used as a measure to estimate the content of paracrystals in the experimental samples. Indeed, the extracted $S(Q)$ of the synthesized samples from the XRDs³⁶ in Figure 1 exhibits exactly the predictive trend, that is, as the annealing temperature increases, the intensity of the first main diffraction peak also increases (Fig. 3b). Plotting I_1/I_2 against paracrystal volume fraction ϕ , we find that high proportions of paracrystals exist in the samples synthesized at temperatures above 1400 K (Fig. 3c). For instance, the amount of paracrystals reaches as high as 52% in the sample synthesized at 1600 K. A satisfactory match between the $S(Q)$ of a paracrystalline model ($\phi = 0.5$) and that of the 1500 K sample is achieved, as demonstrated in Fig. 3d, which presents the structural model of a homogeneous p-D with 70% paracrystals with CD- and HD-like paracrystals ($\sim 0.8\text{-}1.0 \text{ nm}$ in size) with roughly 4 or 5 atomic shells. The simulated HRTEM image of this atomistic model (Fig. 3d) is in striking agreement with the experimental HRTEM images (Fig. 2f), validating the paracrystalline nature of the samples we synthesized.

To further distinguish the structural difference between a-D and p-D and enable identification of CD- or HD-like atomic packing in the as-developed p-D, we employed the common-neighbor analysis (CNA)³⁷ and orientational order analysis (OOA) methods. Here, a-D serves as a reference state to delineate the unique structural features pertaining to p-D. Figure 4a illustrates the atomic structures of p-D and a-D visualized based on their respective degree of MRO, represented by the CNA indices and an orientational order parameter \bar{q}_6 ³⁸. The parameter \bar{q}_6 for a particular atom is a coarse-grained quantity that measures the extent to which the orientation of the atoms in the coordination shells matches the orientation of the central atom, revealing the crystalline MRO. Through CNA, high fractions of CD and HD-like clusters are found to be abundant in p-D, but they are starkly absent in a-D. Moreover, the corresponding atomic structure of p-D visualized by the orientational order parameter \bar{q}_6 reveals the orientational order of the local clusters, supporting the presence of MRO clusters in p-D. Note that the degree of ordering decays gradually

from the central atoms in clusters, suggesting that the paracrystals have a limited spatial length scale. To shed light on the size of the paracrystals, we adopted an orientational correlation function (OCF) $\kappa(r)$. Fig. 4b shows the radial distribution functions (RDFs) $g(r)$ and the orientational correlation functions of p-D and a-D, respectively. Both a-D and p-D have nearly the same $g(r)$ profile for the first peak, in agreement with their respective tetrahedral atomic environments. However, the intensity of the first peak in the $\kappa(r)$ of a-D is significantly lower than that of p-D where just two peaks are visible in the profile, suggesting that a-D has short-range ordering (SRO) within two coordination shells. In contrast, the first five sharp peaks in p-D indicate the strong MRO and the subsequent three peaks are weakened and broadened because of the absence of LRO. For comparison, we also simulated ultrafine nano-polycrystalline diamond (NPD) with different grain sizes (1.20-2.40 nm); there is a completely different morphology in NPD due to the presence of LRO (Extended Data Fig. 4).

We attribute the formation of p-D to two main factors. First, we discovered that the CRN-type a-D exhibits strong diamond-like SRO in the first-two atomic shells (16 atoms). Hence, we devised a local order parameter s to gauge the similarity between the first two atomic shells of each atom of a-D and those of perfect CD or HD crystals (Extended Data Figs. 5 and 6). Inclusion of the second shell in the consideration of the local atomic environment is justified if one is to perform a Voronoi tessellation^{5, 39} to determine atomic coordination. In comparison to other tetrahedral systems such as a-Si, the similarity order parameter of a-D significantly shifts toward high values, signaling much-enhanced SRO within the first-two nearest-neighbor distance. The high similarity of the local atomic environments between a-D and crystalline diamond stems from the strong directional sp^3 bonding of carbon, as evidenced from the narrower bond-angle distribution of a-D in comparison to that of a-Si. This is consistent with the argument that sp^3 carbon has the largest tetrahedral parameter among all group IV elements⁴⁰. The pronounced intrinsic diamond-like SRO of a-D greatly facilitates the development of MRO, and consequently the formation of diamond paracrystals.

Second, the successful synthesis of p-D depends highly on the structure of the C_{60} precursor. We argue that the formation of p-D is a result of a nucleation-controlled process, where the formation of orientationally correlated sp^3 bonds between neighboring C_{60} units offers high-density fertile sites for nucleation. To reveal the effect of the unique structure of C_{60} as a precursor on the synthesis of p-D, we investigated the structural evolution from C_{60} to p-D under HP-HT using both classical MD and *ab initio* MD simulations (see Supplementary Note and Extended Data Figs. 9-13 for details). Our results clearly demonstrate that the formation of p-D goes through three main stages: (i) inter-buckyball bond connection (15% sp^3 bonds) during compression to 30 GPa at room

temperature; (ii) kinetically controlled polymerization and collapse of buckyballs during heating to 1600 K at 30 GPa, where the fraction of sp^3 bonds increases with increasing temperatures; and (iii) the formation of p-D from a-D during isothermal annealing at 1600 K and 30 GPa. In particular, we find that the sp^3 bonds due to inter-buckyball connections in the early stage of polymerization are orientationally ordered in the local contact regions (Extended Data Fig. 10) which persists into the a-D state at high temperatures and contributes to the formation of p-D. Abundant and homogeneous sp^3 bonding of C_{60} by polymerization under high pressure and low temperature prevents the otherwise heterogeneous nucleation and growth of crystals, allowing the formation of p-D in a divide-and-conquer manner. To further understand the critical role of C_{60} in the formation of p-D, we examined other sp^2 -dominated carbons in experiments (carbon onion and type-1 glassy carbon) as a precursor in the same HP-HT conditions, which failed to synthesize p-D in our experiments (Extended Data Fig. 1).

In the MD simulation of p-D, we tracked the trajectories of emerging paracrystals. By studying the appearance and disappearance of the fluctuating crystal embryos (see Supplementary Video), we were able to estimate the critical nuclei size of p-D, which were found to contain approximately 20-30 atoms (~ 3.0 Å), suggesting that the paracrystals belong to supercritical nuclei. Thermodynamically, these supercritical nuclei have certain probabilities of transitioning to amorphous states. Owing to the dynamic fluctuations, the maximum amount of paracrystals is theoretically limited within a certain fraction (i.e., $\phi = 0.7$). Meanwhile, by engaging the similarity order parameter s , the paracrystals were found to be severely distorted in comparison to perfect diamond lattices, of which the level of distortion is on par with the grain-boundary atoms of ultrafine NPD. This accounts for the absence of Bragg diffraction peaks from its XRD pattern.

The unique MRO structures of p-D elicit new physical properties. The mechanical properties of p-D were assessed by the measurements of Vickers' and nanoindentation hardness. p-D exhibits highly isotropous Vickers hardness H_v of 116 GPa and nanoindentation hardness H_N of 105 GPa (Extended Data Fig. 7), superior to that of natural diamond⁴¹. The obtained Young's modulus E (1194 GPa) and shear modulus G (558 GPa) of p-D are greater than those of diamond (1100 GPa and 536 GPa)⁴², making it an appealing candidate for ultra-hard materials. Moreover, a measurement of thermostability of p-D in the air (Extended Data Fig. 8) gives an onset oxidation temperature of 950 K, much higher than those (673-873 K) of DLC films⁴³, nano diamond⁴⁴, CVD diamond⁴⁵ and NPD. These outstanding combinations of mechanical properties and oxidation resistance endow p-D with great potential for niche technological applications. The synthesis of p-D was enabled in a well-controlled near-equilibrium condition, which could be further exploited to obtain novel carbon materials with unusual structural features.

1. R. Zallen, *The physics of amorphous solids* (Wiley, 1983).
2. Zachariasen, W. H. The atomic arrangement in glass. *J. Am. Chem. Soc.* **54**, 3841–3851 (1932).
3. Elliott, S. R. A continuous random network approach to the structure of vitreous boron trioxide. *Philos. Mag. B* **37**, 435–446 (1978).
4. Elliott, S. R. Medium-range structural order in covalent amorphous solids. *Nature* **354**, 445–452 (1991).
5. Sheng, H. W., Luo, W. K., Alamgir, F. M., Bai, J. M. & Ma, E. Atomic packing and short-to-medium-range order in metallic glasses. *Nature* **439**, 419–425 (2006).
6. Miracle, D. B. A structural model for metallic glasses. *Nat. Mater.* **3**, 697–702 (2004).
7. Hirata, A. *et al.* Direct observation of local atomic order in a metallic glass. *Nat. Mater.* **10**, 28–33 (2011).
8. Hirai, H., Kondo, K., Yoshizawa, N. & Shiraishi, M. Amorphous diamond from C₆₀ fullerene. *Appl. Phys. Lett.* **64**, 1797–1799 (1994).
9. Zeng, Z. *et al.* Synthesis of quenchable amorphous diamond. *Nat. Commun.* **8**, 322 (2017).
10. Lin, Y. *et al.* Amorphous diamond: a high-pressure superhard carbon allotrope. *Phys. Rev. Lett.* **107**, 175504 (2011).
11. Treacy, M. M. J. & Borisenko, K. B. The local structure of amorphous silicon. *Science* **335**, 950–953 (2012).
12. Sørensen, S. S., Biscio, C. A. N., Bauchy, M., Fajstrup, L. & Smedskjaer, M. M. Revealing hidden medium-range order in amorphous materials using topological data analysis. *Sci. Adv.* **6**, (2020).
13. Leocmach, M. & Tanaka, H. Roles of icosahedral and crystal-like order in the hard spheres glass transition. *Nat. Commun.* **3**, 1–8 (2012).
14. Gibson, J. M., Treacy, M. M. J., Sun, T. & Zaluzec, N. J. Substantial crystalline topology in amorphous silicon. *Phys. Rev. Lett.* **105**, 1–4 (2010).
15. Oganov, A. R., Hemley, R. J., Hazen, R. M. & Jones, A. P. Structure, bonding, and mineralogy of carbon at extreme conditions. *Rev. Mineral. Geochemistry* **75**, 47–77 (2013).
16. Georgakilas, V., Perman, J. A., Tucek, J. & Zboril, R. Broad family of carbon nanoallotropes: classification, chemistry, and applications of fullerenes, carbon dots, nanotubes, graphene, nanodiamonds, and combined superstructures. *Chem. Rev.* **115**, 4744–4822 (2015).
17. Németh, P. *et al.* Complex nanostructures in diamond. *Nat. Mater.* **19**, 1126–1131 (2020).
18. Sarac, B. *et al.* Origin of large plasticity and multiscale effects in iron-based metallic glasses. *Nat. Commun.* **9**, 1–10 (2018).
19. Hwang, J. *et al.* Nanoscale structure and structural relaxation in Zr₅₀Cu₄₅Al₅ bulk metallic glass. *Phys. Rev. Lett.* **108**, 1–5 (2012).
20. Voyles, P. M. *et al.* Structure and physical properties of paracrystalline atomistic models of amorphous silicon. *J. Appl. Phys.* **90**, 4437–4451 (2001).
21. Robertson, J. Diamond-like amorphous carbon. *Mater. Sci. Eng. R Reports* **37**, 129–281 (2002).

22. Ishii, T., Liu, Z. & Katsura, T. A breakthrough in pressure generation by a Kawai-type multi-anvil apparatus with tungsten carbide anvils. *Engineering* **5**, 434–440 (2019).
23. Iwasa, Y. *et al.* New phases of C₆₀ synthesized at high pressure. *Science* **264**, 1570–1572 (1994).
24. Blank, V. D. *et al.* Phase transformations in solid C₆₀ at high-pressure-high-temperature treatment and the structure of 3D polymerized fullerites. *Phys. Lett. A* **220**, 149–157 (1996).
25. Zhang, S. *et al.* Discovery of carbon-based strongest and hardest amorphous material. Preprint at < <https://arxiv.org/abs/2011.14819> > (2020).
26. Yamanaka, S. *et al.* Electron conductive three-dimensional polymer of cuboidal C₆₀. *Phys. Rev. Lett.* **96**, 076602 (2006).
27. Ferrari, A. C. & Robertson, J. Raman spectroscopy of amorphous, nanostructured, diamond-like carbon, and nanodiamond. *Philos. Trans. R. Soc. London. Ser. A Math. Phys. Eng. Sci.* **362**, 2477–2512 (2004).
28. Daniels, H., Brydson, R., Rand, B. & Brown, A. Investigating carbonization and graphitization using electron energy loss spectroscopy (EELS) in the transmission electron microscope (TEM). *Philos. Mag.* **87**, 4073–4092 (2007).
29. Chen, L. J. *et al.* Structural evolution in amorphous silicon and germanium thin films. *Microsc. Microanal.* **8**, 268–273 (2002).
30. Wang, Q. *et al.* The atomic-scale mechanism for the enhanced glass-forming-ability of a Cu-Zr based bulk metallic glass with minor element additions. *Sci. Rep.* **4**, 1–5 (2014).
31. Tang, H. *et al.* Revealing the formation mechanism of ultrahard nanotwinned diamond from onion carbon. *Carbon* **129**, 159–167 (2018).
32. Plimpton, S. Fast parallel algorithms for short-range molecular dynamics. *J. Comput. Phys.* **117**, 1–19 (1995).
33. Zhu, S. C., Yan, X. Z., Liu, J., Oganov, A. R. & Zhu, Q. A revisited mechanism of the graphite-to-diamond transition at high temperature. *Matter* **3**, 864–878 (2020).
34. Marchi, M. & Ballone, P. Adiabatic bias molecular dynamics: a method to navigate the conformational space of complex molecular systems. *J. Chem. Phys.* **110**, 3697–3702 (1999).
35. L. L. Lee, *Molecular thermodynamics of electrolyte solutions* (World Scientific Publishing, 2008).
36. Sheng, H. W. *et al.* Polyamorphism in a metallic glass. *Nat. Mater.* **6**, 192–197 (2007).
37. Faken, D. & Jónsson, H. Systematic analysis of local atomic structure combined with 3D computer graphics. *Comput. Mater. Sci.* **2**, 279–286 (1994).
38. Lechner, W. & Dellago, C. Accurate determination of crystal structures based on averaged local bond order parameters. *J. Chem. Phys.* **129**, 114707 (2008).
39. Finney, J. L. & A, P. R. S. L. Random packings and the structure of simple liquids. I. The geometry of random close packing. *Proc. R. Soc. London. A. Math. Phys. Sci.* **319**, 479–493 (1970).
40. Hujo, W., Shadrack Jabes, B., Rana, V. K., Chakravarty, C. & Molinero, V. The rise and fall of anomalies in tetrahedral liquids. *J. Stat. Phys.* **145**, 293–312 (2011).

41. Huang, Q. *et al.* Nanotwinned diamond with unprecedented hardness and stability. *Nature* **510**, 250–253 (2014).
42. Teter, D. M. Computational alchemy: the search for new superhard materials. *MRS Bull.* **23**, 22–27 (1998).
43. Bewilogua, K. & Hofmann, D. History of diamond-like carbon films—from first experiments to worldwide applications. *Surf. Coatings Technol.* **242**, 214–225 (2014).
44. Osswald, S., Yushin, G., Mochalin, V., Kucheyev, S. O. & Gogotsi, Y. Control of sp^2/sp^3 carbon ratio and surface chemistry of nanodiamond powders by selective oxidation in air. *J. Am. Chem. Soc.* **128**, 11635–11642 (2006).
45. Pu, J.-C., Wang, S.-F. & Sung, J. C. High-temperature oxidation behaviors of CVD diamond films. *Appl. Surf. Sci.* **256**, 668–673 (2009).

Acknowledgements The authors thank Dr. Ho-kwang Mao for insightful discussions. This work was supported by the National Natural Science Foundation of China (Grants 12075215, 61471307), and was also funded by the European Research Council (ERC) under the European Union's Horizon 2020 research and innovation program (Proposal No. 787527). The work at GMU was supported by the NSF under Grant No. DMR-1611064.

Author contributions H. G. and H. S. proposed and supervised the project; H. T., H. F., T. I., and T. K. synthesized the samples; H. T., X. Y., Y. C., F. L., and M. S. W. performed the structure characterizations; H. T., X. Y., T. L., and Z. Z. measured the properties; H. S. performed the theoretical calculations; H. T., H. S., and H. G. analyzed data and wrote the manuscript with the contributions of all authors.

Competing interests The authors declare no competing interests.

Correspondence and requests for materials should be addressed to H. S. or H. G.

Methods

Sample synthesis

The starting material, C₆₀, was purchased from Alfa Aesar. HP-HT experiments were performed using an ultrahigh-pressure MAP⁴⁶ at Bayerisches Geoinstitut of University of Bayreuth in Germany and the Center for High Pressure Science & Technology Advanced Research (HPSTAR) in China. The synthetic pressure was set to 30 GPa, implemented using carbide anvils with 3-mm truncation and 7-mm MgO + 5 wt.% Cr₂O₃ octahedron. The temperature range was from 1200 to 1800 K, generated using a LaCrO₃ heater. The pressure was calibrated at 2300 K by evaluating the Al₂O₃ content in bridgmanite⁴⁷, and the temperature was monitored using a type-D thermocouple. The starting material was pre-compressed into Pt capsules with diameter of 0.8 and 1.2 mm and height of 1.6 mm. The samples were compressed to 30 GPa and heated to the designated temperatures within a few minutes. *In situ* Raman (532 nm) of C₆₀ under high pressure was conducted by using a symmetrical DAC with a culet size of 300 μm. The samples and ruby spheres for pressure calibration were loaded into the DAC sample chamber with 120 μm in diameter with a pre-indented rhenium gasket without pressure medium.

Structure characterizations

To collect high-quality XRD data, the powder mode of a Bruker D8 Venture diffractometer equipped with Mo K α radiation was employed. The samples were fixed on an organic XRD holder and rotated 720° in total within an acquisition time of 10 min. A background file was obtained with an empty organic holder with the same collection condition. To extract the structure factors from the XRD data, we followed the optimization method proposed in Ref. 36. The microscopic structures of the samples were characterized using an FEI Talos-F200s transmission electron microscope (TEM) operated with an accelerating voltage of 200 keV. The bonding analysis of the samples was done by using Raman and electron energy loss spectroscopy (EELS). The Raman spectra were acquired with two different wavelengths (325 nm and 532 nm) of laser excitation by using a Renishaw-type micro-Raman spectroscopy system. The EELS data were obtained using an ARM-200F (JEOL Ltd.) microscope equipped with a spherical aberration corrector (CEOS GmbH).

Properties measurements

The Vickers hardness H_v was measured using a micro-Vickers hardness tester (Q10A+, Qness GmbH, Austria) with a Vickers diamond indenter at a load of 4.9 N for a holding time of 15 s. H_v was determined from the equation⁴¹ as:

$$H_v = \frac{1854.4F}{L^2} \quad (1)$$

where F (N) is the applied load and L (μm) is the arithmetic mean of the two diagonals of the Vickers indentation.

The nanoindentation hardness (H_N) was measured with a three-sided pyramidal Berkovich diamond indenter (Keysight Nano Indenter G200), and the samples were loaded to the maximum load of 50 mN at a loading rate of 2 mN/s with a holding time of 10 s. The Young's modulus (E) was derived from the loading/unloading-displacement curves according to the Oliver-Pharr method⁴⁸.

The thermostability was evaluated using a thermogravimeter and differential scanning calorimeter, NETZSCHSTA 449 C, from room temperature to 1773 K in the air with a heating rate of 5 K/min.

Computational methods

Structural model of a-D

In this work, a-D was obtained by conducting extensive *ab initio* molecular dynamic (AIMD) simulations, following the protocol introduced in our previous work⁹. In order to yield better statistics, our simulation system was enlarged to 500 carbon atoms. AIMD was performed with the density-functional-theory-based Vienna Ab-initio Simulation Package (VASP)⁴⁹. The projector augmented wave potential (PAW)⁵⁰ with a valence configuration of $2s2p$ and the generalized gradient approximation (GGA) were used in the simulation. The kinetic energy cutoff was set to 400 eV, and the simulation was conducted on the gamma point only. In brief, liquid carbon was slowly quenched from 5000 to 300 K in an NPT (constant number of atoms, pressure and temperature) ensemble under a hydrostatic pressure condition of 50 GPa. The cooling rate was 2.5×10^{13} K/s. A phase transition during the quench process leads to the formation of a-D. The as-obtained high-pressure a-D structure was gradually relaxed to ambient pressure using a conjugate-gradient geometric optimization method. To cross-check the structure resulting from *ab initio* modeling, a different route was employed to generate a-D. In this approach, we applied the bond-switching algorithm⁵¹, also known as the WWW method, to generate ideal CRN configurations with different sizes employing the Keating interatomic potential⁵². The 500-atom CRN structure was further subjected to simulated annealing via *ab initio* MD to minimize local stresses and to achieve a more realistic structural model.

Structural model of p-D and phase transition from C₆₀ to p-D under HP-HT

Both classical MD³² and *ab initio* MD simulations were carried out to study the structure evolution of C₆₀ under high-pressure condition and simulate the formation of p-D. For classical MD, a newly developed angular-dependent interatomic potential (C-ADP)^{33,53} was used to describe carbon. The

development of the realistic C-ADP potential was based on mapping the complex energy landscape obtained with density-functional-theory-based calculations of more than 5000 atomic configurations of C ($>10^6$ atoms in the fitting database)^{54,55}. The empirical potential has been tested to be reliable in describing carbon phase behaviors over a wide temperature and pressure range (0-100 GPa) without compromising the computational speed, enabling us to simulate large samples across an extended temporal scale (in the sub-microsecond regime). The detailed MD simulation steps are given as follows:

- 1) A 36000-atom fcc-C₆₀ crystal was created with C₆₀ buckyballs randomly oriented. The fcc-C₆₀ crystal was equilibrated at 300 K and zero pressure for 1 ns.
- 2) The well-equilibrated C₆₀ crystal was compressed to 30 GPa at room temperature at a constant compression rate of 0.5 GPa/ns.
- 3) The system was brought up to 1600 K at 30 GPa at a constant heating rate of 1.0×10^6 K/s.
- 4) The system was subject to long time annealing at 1600 K and 30 GPa, up to 15 ns.
- 5) The brute-force MD faces great challenges in extending the timescale to minutes (necessary for the formation of p-D). To circumvent this inadequacy, enhanced sampling approaches must be taken. Here, to accelerate the formation kinetics of p-D, an adiabatic-bias molecular method (ABMD) was adopted, which was tested to be a more effective approach than other barrier-crossing techniques such as metadynamics⁵⁶ and the extended Lagrangian method⁵⁷.

In the ABMD simulations stated above, a biasing potential was added to act upon a collective variable, driving the system away from the amorphous state and gearing toward the formation of paracrystals. In this work, the mean value of the order parameter \bar{q}_6 , i.e., $\bar{q}_6^a = \sum_i^N \bar{q}_6^i / N$, was used as a collective variable. The definition of \bar{q}_6^i is given in the following section and N is the total number of atoms in the system. The biasing potential V in the ABMD simulation was constructed as:

$$V[\phi(t)] = \begin{cases} \frac{1}{2}K[\phi(t) - \phi_m(t)]^2 & \text{for } \phi(t) > \phi_m(t) \\ 0 & \text{for } \phi(t) \leq \phi_m(t) \end{cases} \quad (2)$$

where $\phi(t) = [\bar{q}_6^a(t) - \bar{q}_6^t]^2$ and $\phi_m(t) = \min_{0 < \tau < t} \phi(\tau) + \eta(t)$. $\eta(t)$ is a white noise added to the minimum position of the potential. The parameters used in the bias potential were: $K = 5 \times 10^5$ eV and the target order parameter $\bar{q}_6^t = 0.6$. The ABMD method was implemented in the PLUMED package⁵⁸.

To corroborate the classical MD results of C₆₀ collapse and polymerization during the early stage of compression, we also conducted *ab initio* MD simulation to study the phase behavior of fcc-C₆₀

(720 atoms). To this end, the fcc-C₆₀ crystal was first slowly compressed to 30 GPa by geometrical optimization. Then, the phase evolution of the compressed C₆₀ at 30 GPa from 300-1500 K was monitored by conducting *ab initio* NPT simulation at a heating rate of 2×10^{14} K/s.

Structural model of NPD

Classical MD was used to generate atomic structures of NPD. To construct the initial structure, the Voronoi tessellation method was used to generate nearly-equal-sized nanograins with desirable grain sizes (1.2-2.4 nm). The grains were filled with carbon atoms in diamond cubic arrangements. The as-constructed samples, typically consisting of $\sim 100,000$ atoms, were thermally annealed at 1600 K and 30 GPa for 0.2 ns, followed by relaxations to ambient conditions at 300K and 0 GPa. The exact grain size of the NPD was computed post-mortem, based on

$$d = \sqrt[3]{\frac{6 N \cdot \phi}{\pi n_g}} \quad (3)$$

where N is the total number of atoms, ϕ fraction of atoms associated with nanocrystals, and n_g number of grains.

Structural analysis

For short-range ordering, we proposed a local order parameter s to gauge the similarity between the first two atomic shells of each atom of a-D and that of CD or HD crystal. The similarity order parameter s between cluster A and a reference cluster B is defined as:

$$s^B = \max_{l, \alpha, \beta, \gamma} \frac{N_B \sum_i^{N_A} \sum_j^{N_B} \exp[-(\mathbf{T} \cdot \mathbf{r}_i^A - \mathbf{r}_j^B)^2 / \sigma^2]}{N_A \sum_i^{N_B} \sum_j^{N_B} \exp[-(\mathbf{r}_i^B - \mathbf{r}_j^B)^2 / \sigma^2]} \quad (4)$$

where N_A and N_B denote the number of atoms in clusters A and B, respectively; \mathbf{r}_i and \mathbf{r}_j are the cartesian coordinates of the i^{th} and j^{th} atoms in the corresponding cluster; σ is a gaussian smearing parameter, which was set to 0.15 in this work; \mathbf{T} is a transformation matrix that accounts for affine scaling transformation and cluster rotation, where l is a scaling parameter and α, β, γ are Euler angles for rotation. Having obtained s^{CD} and s^{HD} , we define $s = \max(s^{\text{CD}}, s^{\text{HD}})$. Based on the above definition, s lies between 0 and 1 (e.g., two identical clusters would yield $s = 1$ regardless of their respective orientations). A large s value implies a high similarity between the local cluster and the reference crystal, *i.e.*, enhanced short-range ordering. The similarity order parameter also provides a facile tool to quantify lattice distortions of the paracrystals.

For medium-range ordering, a local Steinhardt order parameter \bar{q}_6 was used to evaluate the orientational order associated with each atom, which contains ordering information including a few atomic shells. For atom i , the order parameter \bar{q}_6^i was computed by:

$$\bar{q}_6^i = \sum_j^{N_c} \sum_{m=-6}^{m=6} q_{6m}^*(i) q_{6m}(j) \quad (5)$$

where N_c is the total number of atoms included in the coordination shells (i.e., medium-range clusters, typically up to 4 atomic shells in this work), and $q_{6m}(i)$ is the Steinhardt vector⁵⁹ of atom i , calculated from:

$$q_{6m}(i) = \sum_k^{CN} Y_{6m}(r_{ik}) \quad (6)$$

where k loops over all atoms in the nearest neighbors of atom i (in this work, CN = 4), and Y_{6m} is one of the sixth order spherical harmonics.

While the order parameter \bar{q}_6 yields information about the degree of structural ordering in the system, it is incapable of revealing the exact type of atomic packing (e.g., CD vs. HD). To mitigate this insufficiency, the CNA method was adopted⁶⁰. The second-nearest-neighbors of each atom in cubic diamond have an fcc packing with CNA-index (421), whereas for hexagonal diamond, the 12 second-nearest-neighbors are arranged in an hcp packing which can be differentiated with CNA-index (422) (see Extended Data Figure 6). By performing CNA analysis, each atom can thus be exclusively labeled as the CD-like, HD-like, or disordered type.

Having determined the packing type of the atoms, we used the following algorithm to compute the volume fraction of the paracrystals in the sample, ϕ . Firstly, all atoms identified to have CD- or HD- like packing via CNA analysis, together with their 16 nearest neighbors, are considered as paracrystalline atoms. Secondly, other four-fold coordinated atoms that are directly bonded to the aforementioned paracrystalline atoms are included in the calculation of ϕ , to account for the “boundary” portion of the paracrystals. Following this algorithm, we computed the volume fraction of the crystalline component of NPD ($d = 1.56$ nm) to be 94% for benchmarking.

To mathematically quantify the spatial extension of the paracrystals, we invoked a two-point orientational correlation function (OCF), $\kappa(r)$, given by:

$$\kappa(r) = \left\langle \sqrt{\frac{\sum_{m=-6}^{m=6} q_{6m}(i) \cdot q_{6m}^*(j)}{|\sum_{m=-6}^{m=6} q_{6m}(i)| \cdot |\sum_{m=-6}^{m=6} q_{6m}(j)|}} \delta(r_{ij} - r) \right\rangle \quad (7)$$

where the bracket indicates the calculation is averaged over all atomic pairs. The $\kappa(r)$ essentially measures the orientation relationship of two coordination polyhedral at a distance r . In two limiting cases, $\kappa(r) = 1$ for perfect crystals, and $\kappa(r) = 0$ for totally uncorrelated structures. Empirically, we consider $\kappa(r) = 0.3$ as the threshold to estimate the correlation length of the paracrystals.

Structure factor calculation

Our *ab initio* modeling provides a reliable and predictive structural model for a-D. Nonetheless, the simulated sample has a finite size effect. If $S(Q)$ is calculated based on the Fourier transformation of the pair distribution function $g(r)$, truncation ripples will be inevitably incurred in the calculated $S(Q)$. To circumvent this issue, we accurately calculated the structure factors based on the Ornstein-Zernike (OZ) theory³⁵, which relies on solving for short-ranged direction correlation function $c(r)$ from the OZ equation:

$$h(r) = c(r) + \int dr h(r)c(r) \quad (8)$$

where $h(r) = g(r) - 1$.

In practice, we followed Baxter's factorization⁶¹ method together with Dixon-Hutchinson's numerical algorithm⁶² to obtain $c(r)$ from $g(r)$. Having derived $c(r)$, $S(Q)$ was computed from its Fourier transform $C(Q)$ following:

$$S(Q) = \frac{1}{1 - \rho C(Q)} \quad (9)$$

where ρ is the density. In this way, we were able to accurately analyze the differences between the structure factors of a-D and p-D without being encumbered by artifacts due to the finite size effect.

HRTEM simulation

HRTEM image simulations were performed based on a multi-slice algorithm as implemented in MULTEM⁶³. The sample thickness was typically 80 Å, and a partial coherence illumination mode was used.

Data availability

The data that support the findings of this study are available from the corresponding authors upon request.

Cold availability

The software used for data analysis is available from H.S. upon request.

46. Ishii, T. *et al.* Generation of pressures over 40 GPa using Kawai-type multi-anvil press with tungsten carbide anvils. *Rev. Sci. Instrum.* **87**, 024501 (2016).
47. Kubo, A. & Akaogi, M. Post-garnet transitions in the system $\text{Mg}_4\text{Si}_4\text{O}_{12}$ - $\text{Mg}_3\text{Al}_2\text{Si}_3\text{O}_{12}$ up to 28 GPa: Phase relations of garnet, ilmenite and perovskite. *Phys. Earth Planet. Inter.* **121**, 85–102 (2000).
48. Oliver, W. C. & Pharr, G. M. An improved technique for determining hardness and elastic modulus using load and displacement sensing indentation experiments. *J. Mater. Res.* **7**,

- 1564–1583 (1992).
49. Kresse, G. & Hafner, J. *Ab initio* molecular dynamics for liquid metals. *Phys. Rev. B* **47**, 558–561 (1993).
 50. Blöchl, P. E. Projector augmented-wave method. *Phys. Rev. B* **50**, 17953–17979 (1994).
 51. Wooten, F., Winer, K. & Weaire, D. Computer generation of structural models of amorphous Si and Ge. *Phys. Rev. Lett.* **54**, 1392–1395 (1985).
 52. Keating, P. N. Effect of Invariance requirements on the elastic strain energy of crystals with application to the diamond structure. *Phys. Rev.* **145**, 637–645 (1966).
 53. Mishin, Y., Mehl, M. J. & Papaconstantopoulos, D. A. Phase stability in the Fe–Ni system: Investigation by first-principles calculations and atomistic simulations. *Acta Mater.* **53**, 4029–4041 (2005).
 54. Brommer, P. & Gähler, F. Potfit: effective potentials from ab initio data. *Model. Simul. Mater. Sci. Eng.* **15**, 295–304 (2007).
 55. Cheng, Y. Q., Ma, E. & Sheng, H. W. Atomic level structure in multicomponent bulk metallic glass. *Phys. Rev. Lett.* **102**, 245501 (2009).
 56. Laio, A. & Parrinello, M. Escaping free-energy minima. *Proc. Natl. Acad. Sci.* **99**, 12562–12566 (2002).
 57. Maragliano, L. & Vanden-Eijnden, E. A temperature accelerated method for sampling free energy and determining reaction pathways in rare events simulations. *Chem. Phys. Lett.* **426**, 168–175 (2006).
 58. Colón-Ramos, D. A., La Riviere, P., Shroff, H. & Oldenbourg, R. Promoting transparency and reproducibility in enhanced molecular simulations. *Nat. Methods* **16**, 670–673 (2019).
 59. Steinhardt, P. J., Nelson, D. R. & Ronchetti, M. Bond-orientational order in liquids and glasses. *Phys. Rev. B* **28**, 784–805 (1983).
 60. Stukowski, A. Structure identification methods for atomistic simulations of crystalline materials. *Model. Simul. Mater. Sci. Eng.* **20**, 045021 (2012).
 61. Baxter, R. J. Method of Solution of the Percus-Yevick, Hypernetted-Chain, or Similar Equations. *Phys. Rev.* **154**, 170–174 (1967).
 62. Dixon, M. & Hutchinson, P. A method for the extrapolation of pair distribution functions. *Mol. Phys.* **33**, 1663–1670 (1977).
 63. Lobato, I., van Aert, S. & Verbeeck, J. Progress and new advances in simulating electron microscopy datasets using MULTEM. *Ultramicroscopy* **168**, 17–27 (2016).
 64. Tang, H. *et al.* Synthesis of nano-polycrystalline diamond in proximity to industrial conditions. *Carbon* **108**, 1–6 (2016).

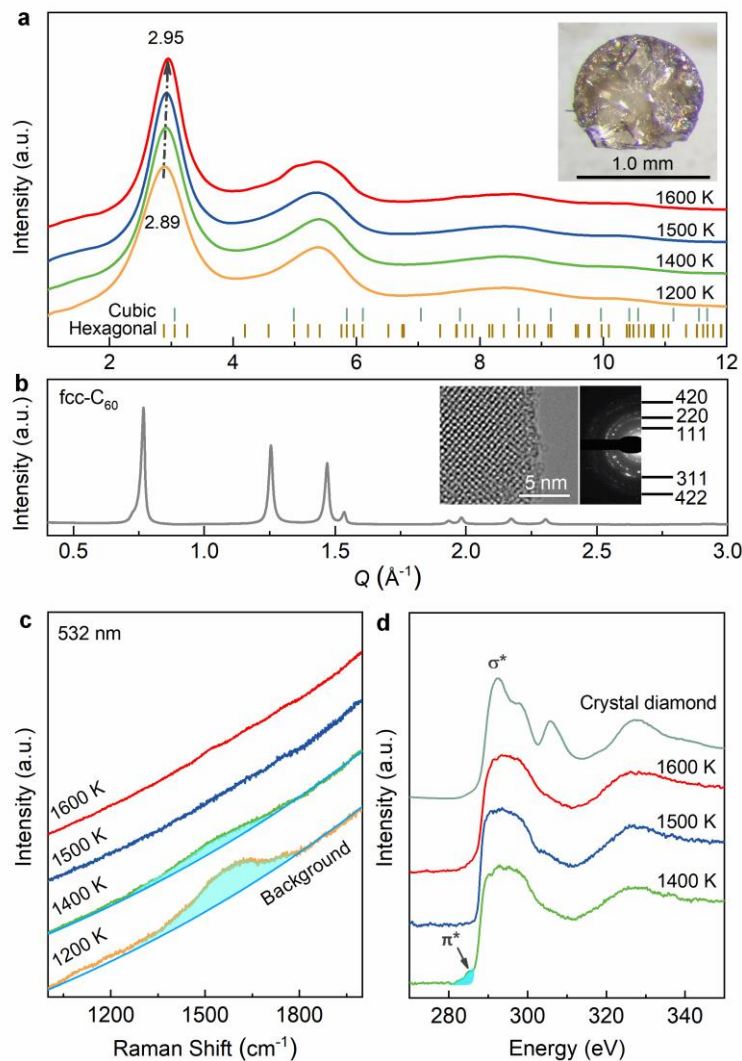


Fig. 1 Synthesizing fully sp^3 -bonded carbon samples at 30 GPa and 1200–1600 K for 10 min. **a**, XRD patterns indicate direct synthesis of disordered carbon from C_{60} under 30 GPa. With increasing temperature, the first main diffraction peak shifts from 2.89 to 2.95 \AA^{-1} , suggesting an increased density at higher temperatures. Inset: a typical optical photograph of the transparent bulk sample (~ 1 mm in diameter) obtained at 30 GPa and 1600 K. **b**, XRD pattern of the C_{60} precursor ($Fm\bar{3}m$). Inset: Corresponding HRTEM image and selected area electron diffraction (SAED) pattern. **c**, Visible Raman (Wavelength of 532 nm) spectra of samples recovered from different temperatures. The samples annealed at 1200 K and 1400 K have similar Raman features with the DLC films having a high sp^3 fraction²⁷, suggesting a trace amount of sp^2 carbon remaining in these samples. **d**, EELS spectra of samples recovered from different temperatures and cubic diamond crystal. The features at 285 and 292 eV are due to transitions of 1s electron to π^* and σ^* , corresponding to sp^2 and sp^3 bonding, respectively. The 1400 K sample has a residual 5.2% of sp^2 bonding, analyzed from the ratio of π^* and σ^* features using single-crystal graphite for calibration²⁸.

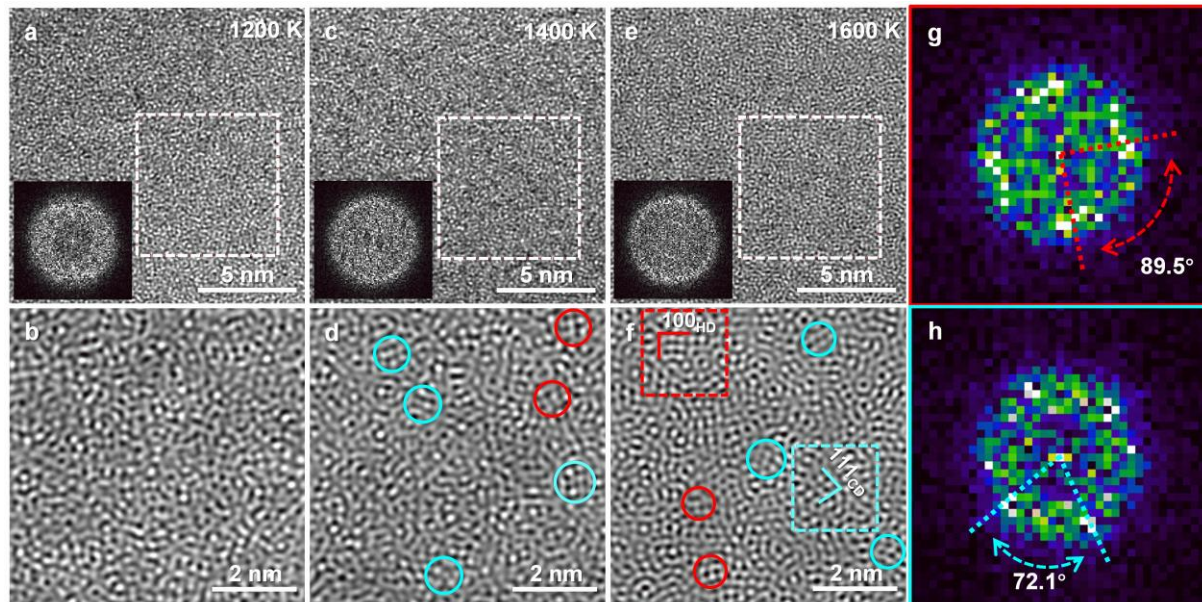


Fig. 2 TEM characterization of samples recovered from 30 GPa and 1200-1600 K. **a-b, c-d, and e-f,** Typical HRTEM images of samples and the corresponding inverse FFT images, respectively. Insets: FFT patterns corresponding to the white boxes ($7.0 \times 7.0 \text{ nm}^2$) in **(a)**, **(c)**, and **(e)**, respectively. The cyan and red circles in **(d and f)** indicate crystal-like MRO clusters. Note that the circles only serve as a guide for the eye. MRO clusters are discernable in **(f)**, where the lattice fringes marked by the cyan and red solid lines match CD- and HD-like (111) and (100) crystal planes, respectively. **g-h,** FFT patterns, corresponding to the red and cyan boxes ($2.0 \times 2.0 \text{ nm}^2$) in **(f)**, respectively. The brighter spots on the diffuse halos indicated by the colored arrows confirm the existence of CD and HD-like MRO clusters illustrated in **(f)**.

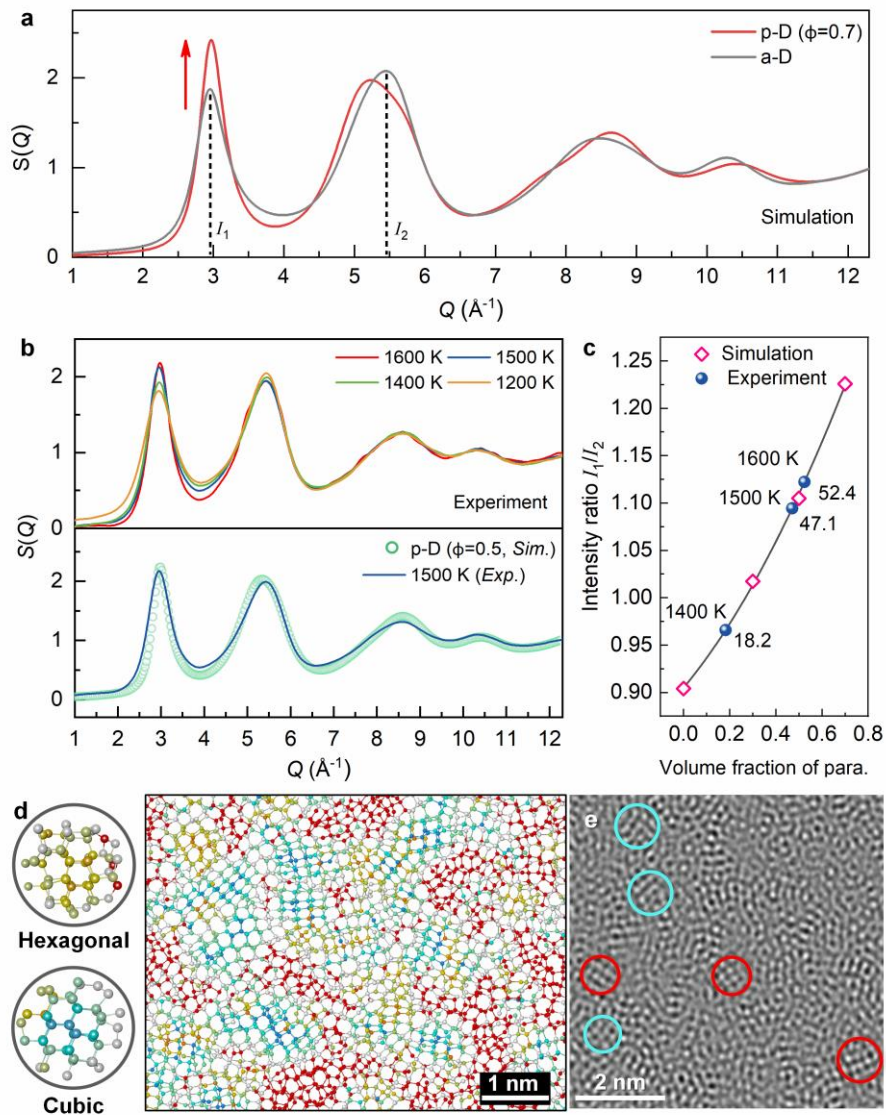


Fig. 3 Identification of p-D. **a**, Simulated structure factor $S(Q)$ of a-D and p-D ($\phi = 70\%$). **b**, Top: Experimental $S(Q)$ of the recovered samples. Bottom: Simulated $S(Q)$ of p-D with 50% paracrystals in comparison to the experimental data. **c**, Intensity ratio of the first peak ($\sim 2.9 \text{ \AA}^{-1}$) to the second peak ($\sim 5.4 \text{ \AA}^{-1}$) as a function of volume percentage of paracrystals. **d**, Structural model of p-D with 70% paracrystals from MD simulation. Colors represent different types of atomic packing. Based on CNA analysis, the turquoise, gold, and red atoms represent CD-, HD-like, and disordered atomic packing within two atomic shells, respectively. The typical size and atomic arrangement of the paracrystals are illustrated in the circles on the left. **e**, Simulated HRTEM image from the paracrystalline model presented in **(d)**. The cyan and yellow circles indicate CD and HD-like clusters, respectively, in agreement with the experimental HRTEM image shown in **Fig. 2f**.

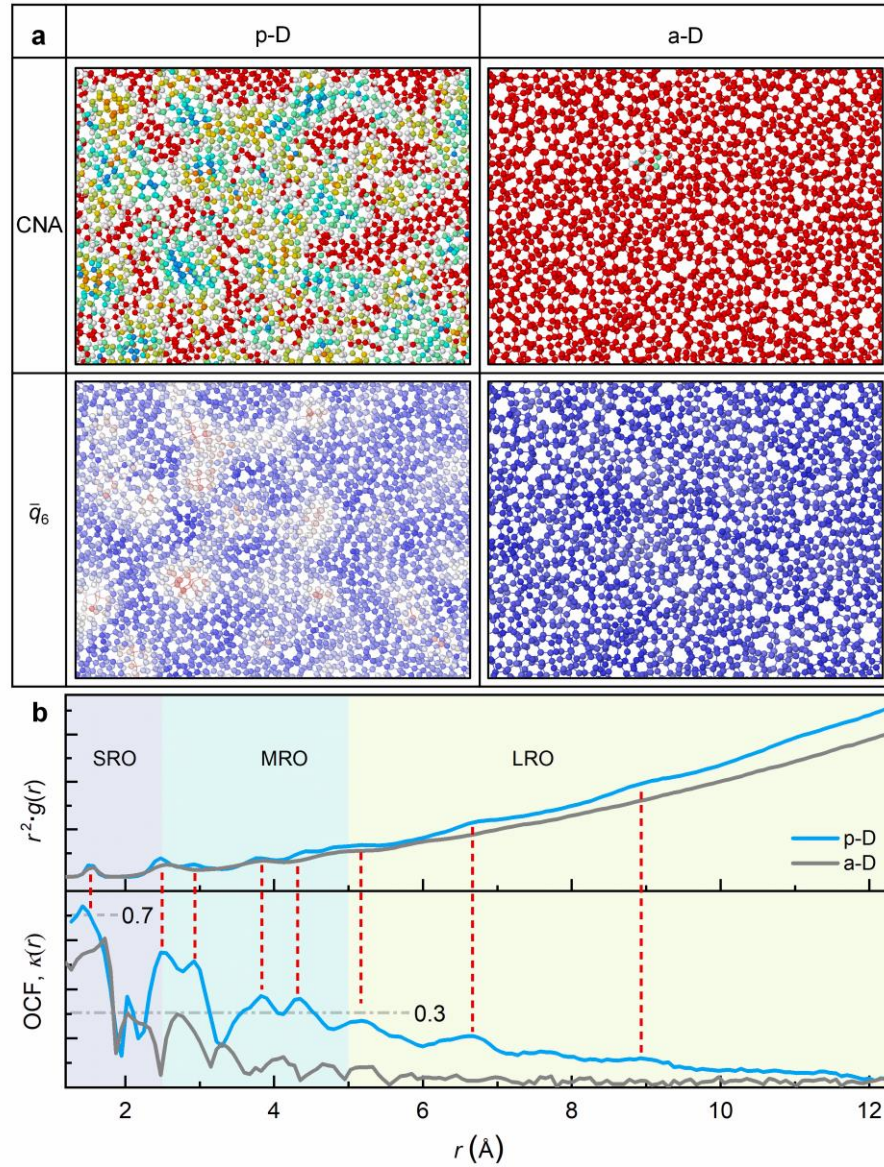


Fig. 4 Distinguishing p-D from a-D. **a**, Atomic structure of p-D vs. a-D, visualized based on their respective degree of MRO represented by the CNA index and orientational order parameter \bar{q}_6 . For a-D, the images present monotonous colors (red and blue), indicating the absence of crystal-like MRO clusters. In contrast, high-fraction MRO CD and HD-like clusters populate and become the main feature in p-D. **b**, The radial distribution function $g(r)$ (top) and orientational correlation function $\kappa(r)$ (bottom) of p-D and a-D, respectively.

Figures

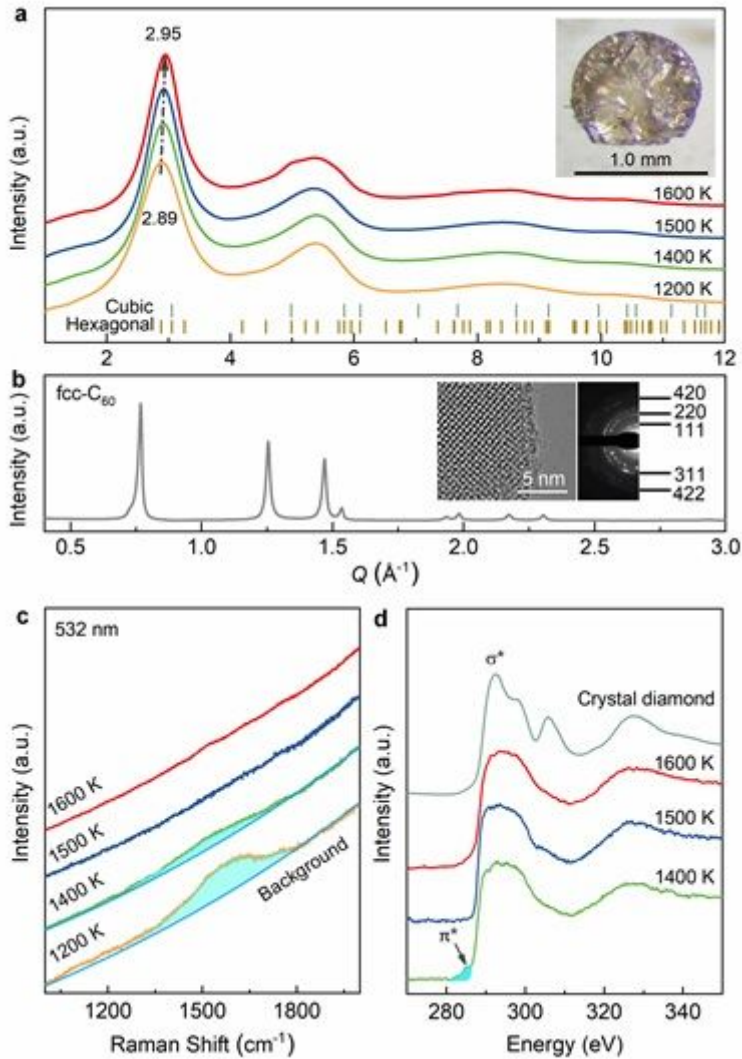


Figure 1

Synthesizing fully sp^3 -bonded carbon samples at 30 GPa and 1200–1600 K for 10 min. a, XRD patterns indicate direct synthesis of disordered carbon from C_{60} under 30 GPa. With increasing temperature, the first main diffraction peak shifts from 2.89 to 2.95 \AA^{-1} , suggesting an increased density at higher temperatures. Inset: a typical optical photograph of the transparent bulk sample (~ 1 mm in diameter) obtained at 30 GPa and 1600 K. b, XRD pattern of the C_{60} precursor ($Fm\bar{3}m$). Inset: Corresponding HRTEM image and selected area electron diffraction (SAED) pattern. c, Visible Raman (Wavelength of 532 nm) spectra of samples recovered from different temperatures. The samples annealed at 1200 K and 1400 K have similar Raman features with the DLC films having a high sp^3 fraction²⁷, suggesting a trace amount of sp^2 carbon remaining in these samples. d, EELS spectra of samples recovered from different temperatures and cubic diamond crystal. The features at 285 and 292 eV are due to transitions of 1s electron to π^* and σ^* , corresponding to sp^2 and sp^3 bonding, respectively. The 1400 K sample has a residual 5.2% of sp^2 bonding, analyzed from the ratio of π^* and σ^* features using single-crystal graphite for calibration²⁸.

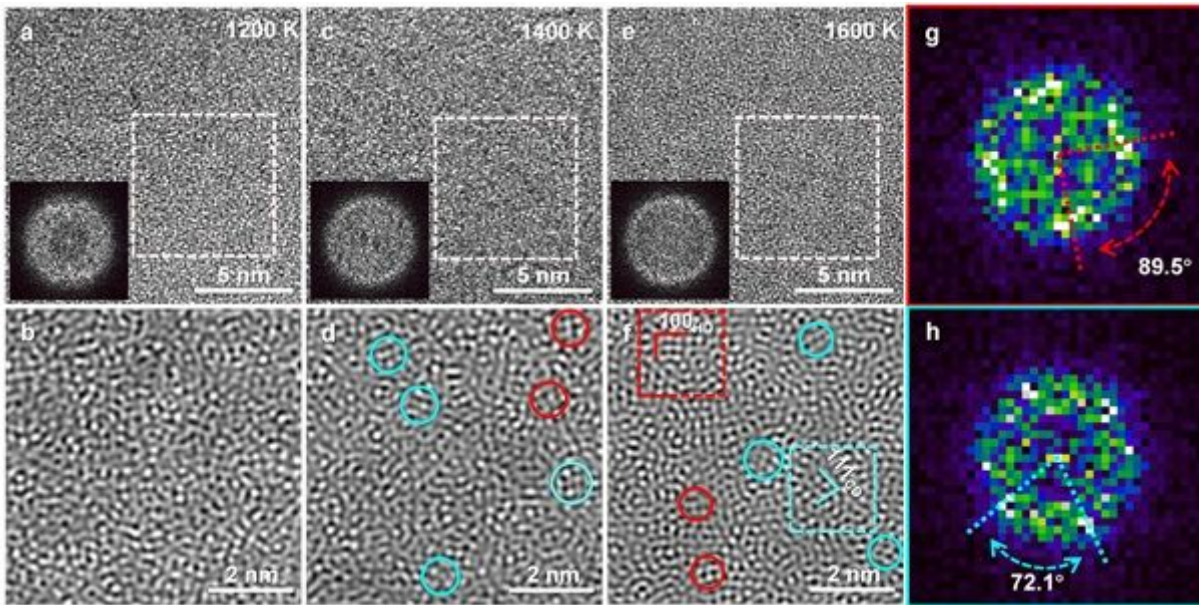


Figure 2

TEM characterization of samples recovered from 30 GPa and 1200-1600 K. a-b, c-d, and e-f, Typical HRTEM images of samples and the corresponding inverse FFT images, respectively. Insets: FFT patterns corresponding to the white boxes ($7.0 \times 7.0 \text{ nm}^2$) in (a), (c), and (e), respectively. The cyan and red circles in (d and f) indicate crystal-like MRO clusters. Note that the circles only serve as a guide for the eye. MRO clusters are discernable in (f), where the lattice fringes marked by the cyan and red solid lines match CD- and HD-like (111) and (100) crystal planes, respectively. g-h, FFT patterns, corresponding to the red and cyan boxes ($2.0 \times 2.0 \text{ nm}^2$) in (f), respectively. The brighter spots on the diffuse halos indicated by the colored arrows confirm the existence of CD and HD-like MRO clusters illustrated in (f).

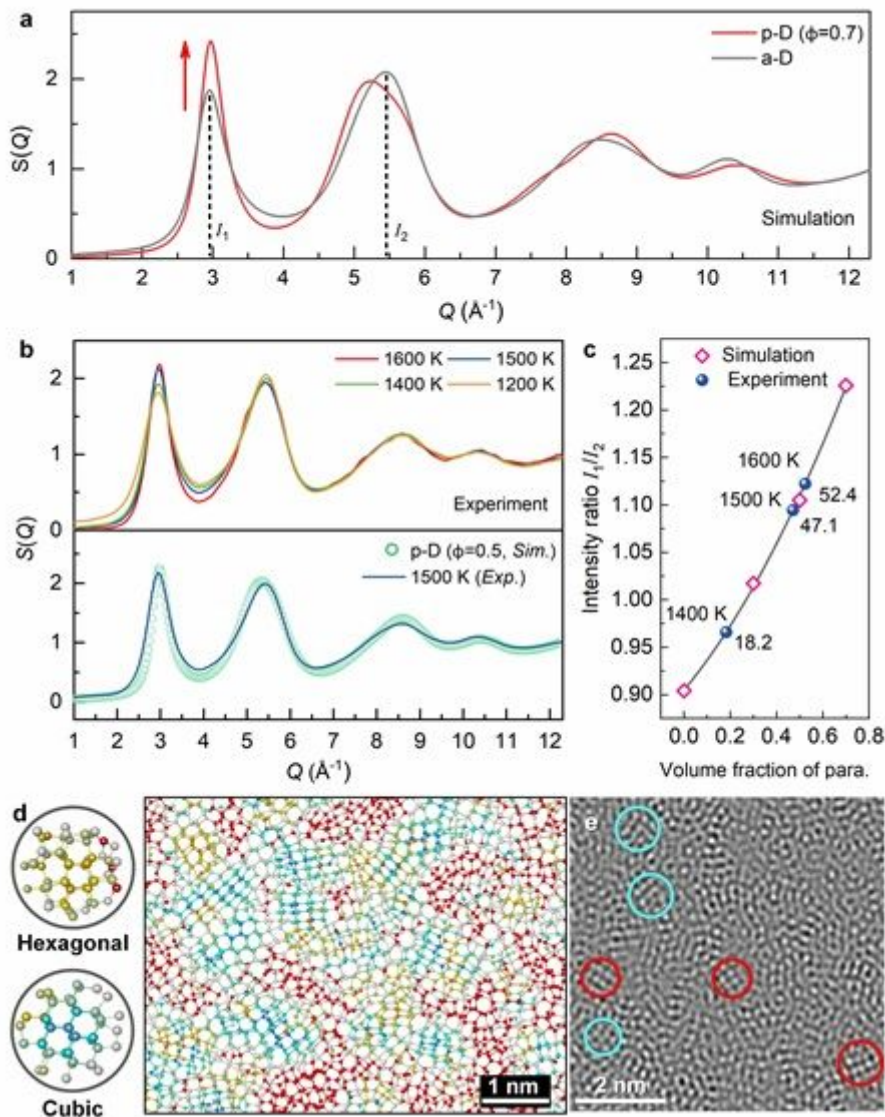


Figure 3

Identification of p-D. a, Simulated structure factor $S(Q)$ of a-D and p-D ($f = 70\%$). b, Top: Experimental $S(Q)$ of the recovered samples. Bottom: Simulated $S(Q)$ of p-D with 50% paracrystals in comparison to the experimental data. c, Intensity ratio of the first peak ($\sim 2.9 \text{ \AA}^{-1}$) to the second peak ($\sim 5.4 \text{ \AA}^{-1}$) as a function of volume percentage of paracrystals. d, Structural model of p-D with 70% paracrystals from MD simulation. Colors represent different types of atomic packing. Based on CNA analysis, the turquoise, gold, and red atoms represent CD-, HD-like, and disordered atomic packing within two atomic shells, respectively. The typical size and atomic arrangement of the paracrystals are illustrated in the circles on the left. e, Simulated HRTEM image from the paracrystalline model presented in (d). The cyan and yellow circles indicate CD and HD-like clusters, respectively, in agreement with the experimental HRTEM image shown in Fig. 2f.

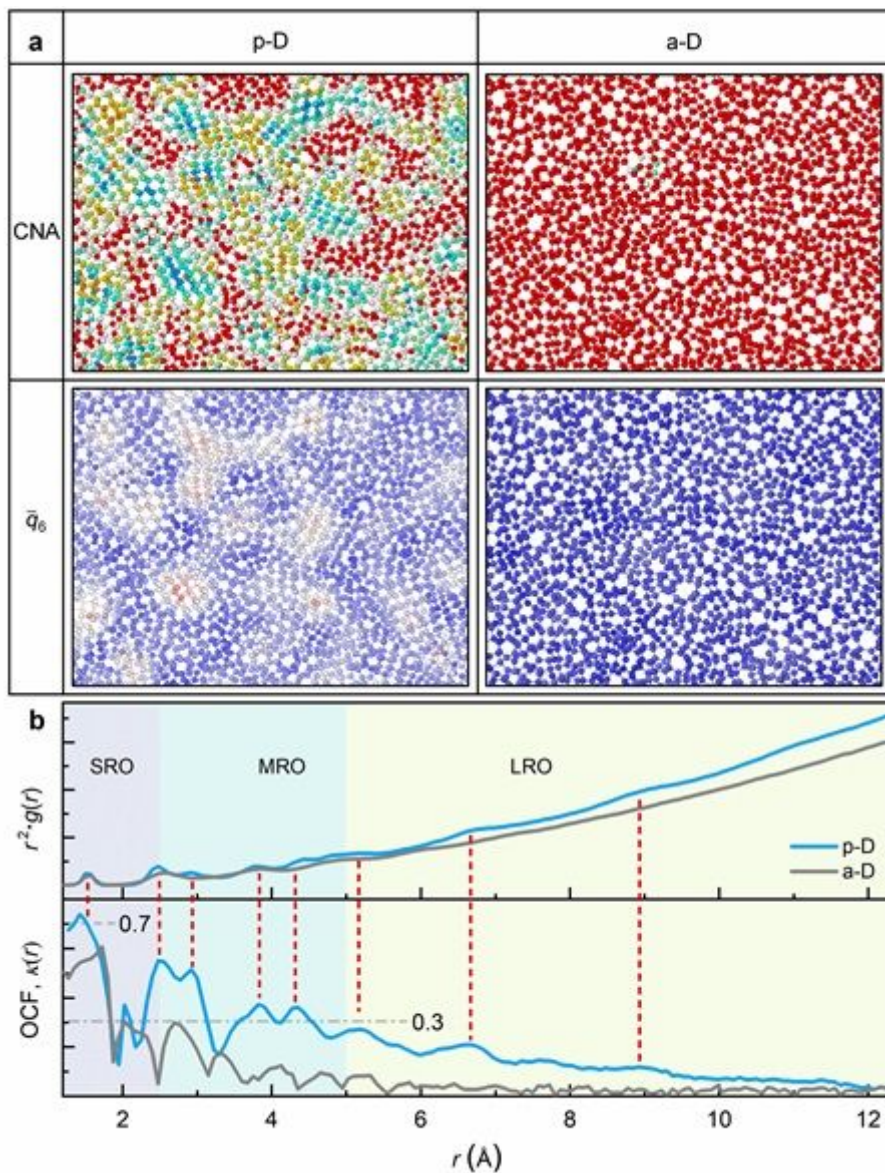


Figure 4

Distinguishing p-D from a-D. a, Atomic structure of p-D vs. a-D, visualized based on their respective degree of MRO represented by the CNA index and orientational order parameter. For a-D, the images present monotonous colors (red and blue), indicating the absence of crystal-like MRO clusters. In contrast, high-fraction MRO CD and HD-like clusters populate and become the main feature in p-D. b, The radial distribution function (top) and orientational correlation function (bottom) of p-D and a-D, respectively.

Supplementary Files

This is a list of supplementary files associated with this preprint. Click to download.

- [SI202104019.docx](#)
- [ExtendedDataFigures202104019.docx](#)
- [GrowingMROwithannealingtimeat1600K30GPa.mp4](#)